RESEARCH ARTICLE

Key Points:
- Injecting sand-fiber suspensions into fractures leads to heterogeneous distribution of solids
- Isolated sand-fiber pillars support normal stress acting on fracture surfaces
- Fluid flow through stressed fracture mobilizes solids forming conductive channels

Supporting Information:
- Supporting Information S1

Correspondence to:
R. L. Detwiler,
detwiler@uci.edu

Settling and Mobilization of Sand-Fiber Proppants in a Deformable Fracture

Ricardo Medina[1] [ID] **, Russell L. Detwiler[1]** [ID] **, Romain Prioul[2]** [ID] **, Wenyue Xu[2]** [ID] **, and Jean E. Elkhoury[2]** [ID]

[1]Department of Civil and Environmental Engineering, University of California, Irvine, CA, USA, [2]Schlumberger-Doll Research Center, Cambridge, MA, USA

Abstract We investigated the response of a sand-fiber proppant suspension (17.7% 40/70 mesh sand and 0.4% polymeric fibers) flowing and settling inside a transparent deformable 15 ×15-cm fracture subjected to an increasing applied normal stress, σ_n. We quantified the solid distribution within the fracture and the evolution of the solid volume fraction, ϕ, as σ_n increased. The sand-fiber suspension formed a highly heterogeneous proppant pack with sand-fiber clumps surrounded by relatively solids-free regions, which was significantly different from the uniform solid distribution observed in settling experiments without fibers. As σ_n increased from 0 to 88.5 kPa, the fracture aperture decreased by up to 85% and caused the sand-fiber clumps to act like pillars that supported the applied stress and prevented full fracture closure. At the end of the settling experiments, we simulated flowback by injecting solids-free carrier fluid while maintaining σ_n = 88.5 kPa. Subsequent flow of solids-free fluid caused the mobilization of some solids but left the supporting pillars intact. We used a numerical model to simulate flow through the porous proppant pack and open regions of the fracture and found a correlation between ϕ and the shear rate, $\dot{\gamma}$, at locations of mobilized solids, which suggested a mobilization threshold: $\phi < \phi_{\text{mob}}$ and $\dot{\gamma} > \dot{\gamma}_{\text{mob}}$. Additional simulations carried out in different heterogeneous proppant distributions showed that solid mobilization leads to the formation of highly conductive channels that significantly increase fracture permeability. Our results suggest that adding fibers to conventional sand proppants can lead to heterogeneous proppant distributions and increased fracture permeability.

1. Introduction

Hydraulic fracturing is an approach for inducing fractures in both rock and unconsolidated sedimentary formations. Fractures are created by injecting large volumes of fluid into the formation at pressures sufficiently greater than the minimum compressive stress to induce tensile fractures. This technique has been widely applied for hydraulic fracturing in the oil and gas industry (Economides & Nolte, 2000) where solid particles (proppants) suspended in a viscous carrying fluid are injected into induced fractures. As fluid pressure in the fracture decreases, the stress acting normal to the fracture surfaces is supported by the proppants. More recently, proppants have been used for enhanced geothermal systems (Shiozawa & McClure, 2016), contaminant remediation (Murdoch et al., 2006) and as a means to increase ground elevations to combat coastal flooding (Germanovich & Murdoch, 2010). A fundamental challenge to effective hydraulic fracturing is maximizing fracture permeability during the proppant placement phase and maintaining it during the production phase as pore pressure decreases.

The permeability of propped hydraulic fractures depends on the fracture aperture, proppant properties, formation strength, and closure pressure (Economides & Nolte, 2000). Efforts to increase fracture permeability have largely focused on carrier fluid and proppant properties (Barbati et al., 2016; Montgomery, 2013; Osiptsov, 2017). In particular, adding polymers to the water-based carrier fluid (e.g., guar gum or xanthan gum) yields a shear-thinning fluid with increased viscosity at low shear rates, thereby reducing particle settling rates (Amundarain et al., 2009; Chudzikowski, 1971; Lei & Clark, 2007; Liu & Sharma, 2005; Metzner, 1985). By increasing the solids carrying capacity of the carrier fluid, it is possible to deliver more proppant to individual fractures, resulting in larger fracture apertures that are completely filled with sand (Medina et al., 2016).

Recent studies have proposed adding polymeric fibers to proppant suspensions in an effort to improve the efficiency of delivering proppant to fractures (Bulova et al., 2006; Gillard et al., 2010; Vasudevan et al., 2001).

Fibers have been shown to increase the apparent fluid viscosity (George et al., 2011, 2012; Guo et al., 2005; Rajabian et al., 2008) and reduce particle settling velocities (Férec et al., 2008; George et al., 2011; Guo et al., 2005). Furthermore, experiments of fiber suspensions have demonstrated the formation of fiber *flocs*, or agglomerations of fibers, when the suspension is subjected to shear deformation (Herzhaft et al., 1996; Schmid et al., 2000). These flocs form even if attractive forces between fibers are ignored, suggesting that the main mechanisms affecting the formation of fiber flocs are the mechanical contacts and hydrodynamic interactions between fibers (Herzhaft et al., 1996). Thus, floc formation depends on the aspect ratio and flexibility of the fibers and the solid content of the fluid-fiber suspension (Herzhaft et al., 1996). Furthermore, experimental observations have shown that floc formation is enhanced for fibers suspended in polymeric solutions, such as guar-water mixtures (Guo et al., 2015) resulting in reduced settling velocities for single particles in suspensions of dispersed fibers (Elgaddafi et al., 2012; Guo et al., 2005; Rajabian et al., 2008). The formation of these fiber flocs appears to be a promising mechanism to reinforce proppant packs (Potapenko et al., 2014; Willberg et al., 2011); however, further studies on the interactions of sand-fiber mixtures are needed.

The tendency of fibers to flocculate in a suspension can promote formation of a heterogeneous distribution of solids within fractures (Medvedev et al., 2013). This has the potential to result in localized regions of highly concentrated sand and fibers separated by regions with little to no solids. When the effective stress acting on the fracture surfaces increases, these localized regions of high-solids content may act as pillars to support the fracture surfaces while the regions between the pillars remain devoid of solids and act as high-transmissivity flow channels (Howard et al., 1999; Morris et al., 2014). This has two distinct advantages over conventional proppant injection techniques: reduced amounts of sand required to prop fractures and enhanced fracture transmissivity. Hydraulic fracturing uses significant quantities of sand; for example, in the Marcellus formation in the United States, on average, $2.1 \cdot 10^6$ kg of sand is injected per well (Edwards & Celia, 2018). If sand can be effectively deposited in localized regions, this quantity can be significantly reduced. In a fracture filled completely with sand, the fracture permeability is controlled by the permeability of the proppant pack. However, in a fracture with localized regions of proppant, the permeability will be controlled by the fracture aperture and connectivity of the surrounding sand-free regions and may be significantly larger than a uniformly sand-filled fracture. These potential benefits of fiber-sand proppant injection require that the localized regions of proppant persist after stress is applied to the propping pillars and that interconnected channels develop during proppant injection or during flowback.

We investigated the behavior of a mixed sand-fiber suspension as it flowed and settled inside a laboratory-scale transparent fracture confined in a rigid frame capable of applying a normal stress, σ_n, to the fracture surfaces. Transmitted light techniques allowed visualization of proppant settling and the subsequent response to applied stresses. We developed a method to estimate solid volume fraction, ϕ_s (volume of solids/total volume), using transmitted light techniques. The experiments show that adding fibers led to the formation of fiber clumps with sand particles entangled within these clumps as suggested by Willberg et al. (2011) and Potapenko et al. (2014). These sand-fiber clumps led to a heterogeneous distribution of settled solids throughout the fracture, which was significantly different than the uniform solid distribution observed in previous settling experiments without fibers. Increasing σ_n led to a decrease in fracture aperture and caused the sand-fiber clumps to act as pillars capable of supporting the applied stress and preventing fracture closure. During the flowback experiment, under an applied normal stress, we observed the mobilization of some solids, many of which were flushed out of the fracture. Using a numerical solver, we simulated flow through the heterogeneous solid distribution and explored the mechanisms controlling solid mobilization and the potential for solid mobilization to further enhance fracture permeability.

2. Methods

Experiments were carried out in a transparent fracture, which allowed visualization of the sand-fiber proppant as it flowed into the fracture, settled between the fracture walls, and deformed due to applied normal stresses. Here we describe the experimental setup, the procedure used to carry out the experiments, and the image processing techniques.

2.1. Experimental Setup

The settling experiments were carried out inside a transparent analog fracture oriented vertically. The experimental setup included a rotating stand supporting a high-resolution charge-coupled-device (CCD) camera (Quantix KAF-6303e), red LED backlight panel (with an emitted light wavelength of $\lambda \approx 625$ nm), electronic
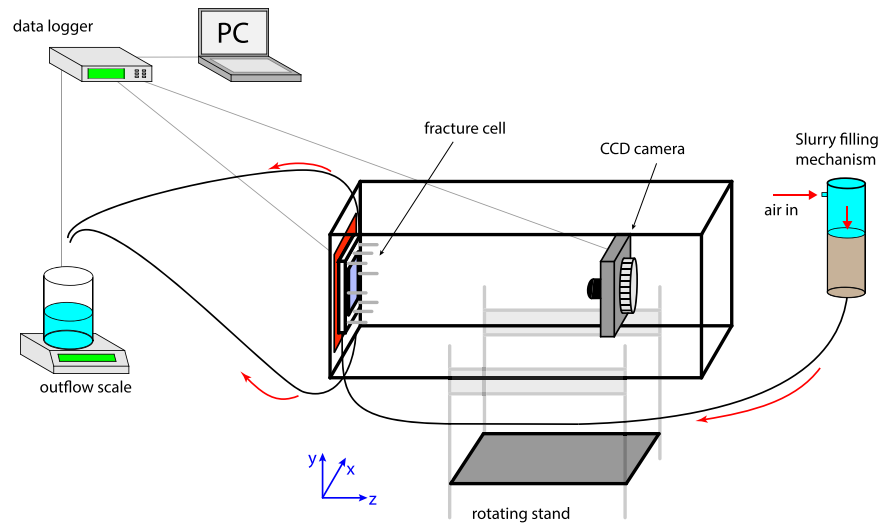
Figure 1. Schematic of experimental system. The slurry-filling mechanism consisted of a pneumatic tank, a PVC pipe with a fitted funneled end cap. After the slurry was poured into the pneumatic tank, the tank was sealed and pressurized air was supplied, which displaced the slurry out of the tank and into the fracture. Once a steady state flow rate was achieved, the flow was stopped and slurry allowed to settle inside the fracture cell (See Figure 2 for details). After the slurry settled for some predetermined time, a normal stress was applied to the fracture cell by activating the pneumatic actuators.

controllers, and the fracture cell (Figure 1). We used a pneumatic tank to inject the suspension into the fracture. The pneumatic tank consisted of a polyvinyl-chloride (PVC) pipe with a fitted funnel bottom cap, an air inlet on the top, and a threaded cap. The tank was sealed after pouring the suspension into the tank; supplying compressed air at the top displaced the suspension out of the tank and into the fracture (Figure 1). A laboratory balance measured effluent mass flow rate.

The transparent fracture was composed of two $15.2 \times 15.2 \times 1.2$-cm flat pieces of glass sealed by two no-flow manifolds (top and bottom), inlet (left), and outlet (right) manifolds (Figure 2). Initial fracture aperture was created by separating the fracture surfaces using removable plastic shims; a normal force was applied to the no-flow manifolds by the screws attached to the outer steel frame. Once the normal force on the side
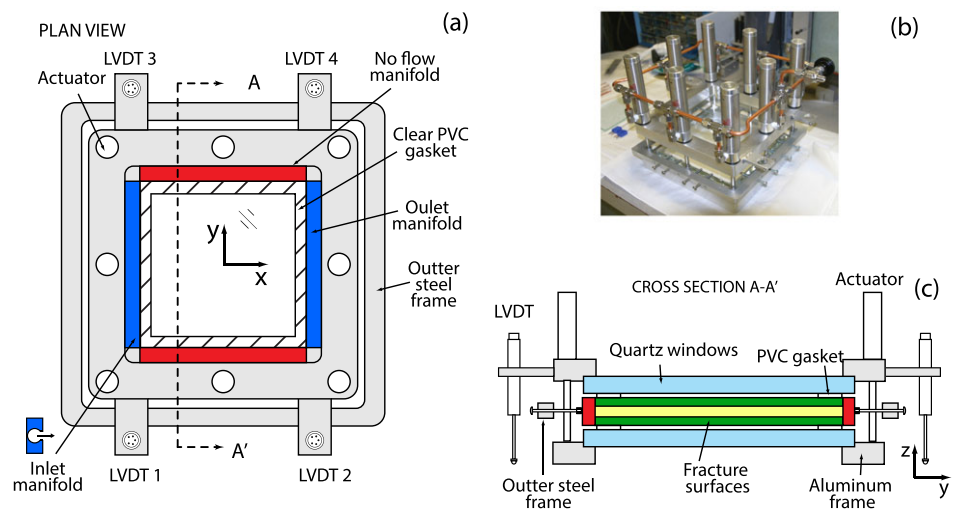

Figure 2. Schematic and photograph of the fracture cell used in our experimental system. (a) Plan view of the fracture cell showing the location of all eight pneumatic actuators, LVDTs, and inlet and outlet manifolds. (b) Photograph of the fracture cell. (c) Cross-section view (A-A') of the fracture cell showing the fracture walls and inlet/outlet manifold configuration. For all experiments, flow was along the x axis and gravity points in the negative y direction. LVDT = linear variable displacement transducer.

Table 1
Summary of Experimental Procedure

	Test A	Test B	Test C
Assemble fracture			
Aperture mean (standard deviation; mm)	3.11 (0.12)	2.87 (0.17)	2.69 (0.11)
Prepare suspension			
Carrier fluid	0.48% by weight guar-water gum mixture		
Sand	40/70 mesh sand, particle radius range: $r = 0.13 - 0.24$ mm ($\phi_s = 0.177$)		
Polymeric fibers	Mean diameter, $d_f = 0.012$ mm and length, $l_f = 10.0 \pm 2.0$ mm ($\phi_f = 0.004$)		
Inject suspension	1. Fill fracture with guar-water carrier fluid		
	2. Inject suspension into fracture at ~400 ml/min for ~5 min		
	3. Cease flow and allow settling for ~15 min		
Apply normal stress	4. Incrementally increase σ_n at ~60-min intervals		
	σ_n intervals: 0, 12.6, 25.3, 37.9, 50.6, 63.2, 75.9, and 88.5 kPa		
Flowback	5. Inject solids-free carrier fluid through proppant pack at $\sigma_n = 88.5$ kPa		
	Approximately 1,000 ml of carrier fluid injected during each flowback stage		
	$Q = 100$ ml/min (2x)	$Q = 100$ ml/min (3x)	$Q = 100$ ml/min (3x)
	$Q = 200$ ml/min	$Q = 250$ ml/min (2x)	$Q = 300$ ml/min (2x)
		$Q = 300$ ml/min	

manifolds was enough to support the fracture surfaces, the plastic shims were removed, and we sealed the fracture using the inlet/outlet manifolds. Because the shims supporting the fracture surfaces needed to be removed prior to applying the inlet/outlet manifolds, some small variability ($\pm5\%$) in the initial mean aperture occurred between experiments (Table 1). The glass fracture surfaces were connected to the fused-quartz windows by a clear PVC gasket. Eight reverse action pneumatic actuators (Bimba SR-092-R) were rigidly mounted on the top aluminum frame with the steel rod threaded to the bottom aluminum frame. The actuators were connected to a manifold ensuring that the applied air pressure was distributed uniformly to all actuators. The air supplied to the actuator cylinder forced the steel rod to move into the cylinder, forcing fracture closure by lowering the top aluminum frame toward the bottom frame which was secured to the imaging stand. Four linear variable displacement transducers (LVDTs, Schaevitz HCD 250) rigidly mounted on opposite sides (two on each side) of the fracture cell accurately (±1 μm) measured displacement of the upper aluminum frame throughout the experiment (Figure 2).

2.2. Experimental Procedure

The carrier fluid was prepared by mixing deionized de-aired water, guar gum (0.48% W/W), and glutaralde-hyde (0.01% V/V) in a laboratory-grade blender for ~15 min. The carrier fluid was then placed under vacuum for 12 hr to remove air bubbles trapped during the mixing process. A detailed description of the preparation method for the carrier fluid was provided by Medina et al. (2015). We used a flat-plate viscometer to measure the viscosity of the guar-water mixture. The fluid exhibits a pseudo plastic shear-thinning behavior with an apparent viscosity of $\eta_o = 2.8$ Pa·s in the low shear rate regime, that is, in the Newtonian regime. The shear-thinning viscosity can be modeled using the non-Newtonian, Ellis model given by

$$\eta(\tau) = \frac{\eta_o}{1 + \left(\tau/\tau_{1/2}\right)^{\beta-1}} \tag{1}$$

where $\tau_{1/2}$ is the shear stress where $\eta = \eta_o/2$. Using a least squares fit of equation (1) to the measured data resulted in estimates of $\tau_{1/2} = 5.76$ Pa and $\beta = 3.30$.

The sand-fiber suspension was prepared by slowly adding 40/70 mesh silica sand (particle radius ranging from $r = 0.13$ to 0.24 mm) and polymeric fibers (fiber length $l_f \approx 10 \pm 2$ mm and diameter $d_f \approx 0.012 \pm 0.002$ mm) into the carrier fluid using a rotary mixing paddle. The suspension was prepared by initially adding ~30% of the total sand and slowly adding fibers while the rotary paddle mixed the suspension. After adding approximately two thirds of the fibers to the suspension, we added additional ~30% of sand, mixed for several minutes, and, finally, added the remaining fibers and sand. Adding solids in small amounts, before and during the fiber mixing process, helped disperse the fibers within the suspension. The final suspension had a total solid

volume fraction of $\phi_{total} = \phi_s + \phi_f = 0.1808$, with most of the solid volume fraction made up of sand particles ($\phi_s = 0.177$) and fibers making up the remainder of the solid volume fraction ($\phi_f = 0.0038$).

We carried out three different experiments (referred to in the text as Tests A, B, and C) to investigate the settling behavior of sand-fiber suspensions (Table 1). To explore reproducibility, all experiments were initialized using the same procedure, which we briefly summarize here. Initially, the fracture and all the tubes were filled with carrier fluid. We acquired a set of reference images with the cell completely filled with carrier fluid. Image acquisition began before injecting the suspension to capture the entire process, that is, initial filling and settling. Immediately after mixing, the suspension was transferred to a pneumatic tank and injected into the fracture at a flow rate of ∼400 ml/min until ∼10 fracture volumes had passed through the system (about 5 min). We allowed the suspension to settle uninterrupted for approximately 25 min before applying a normal stress. We incrementally increased the normal stress, σ_n, at regular time intervals of ∼50 min, from 12.6 kPa up to a maximum of 88.5 kPa. Each actuator applied the same force to the aluminum frame, which was about 0.82 of the supplied air pressure. We assumed that the total force was uniformly distributed on the fracture surface. Reported σ_n values are the uniform stress on the fracture, which was calculated by adding the forces from the eight actuators and dividing by the area of the fracture surface. At the end of the settling experiment, while maintaining $\sigma_n = 88.5$ kPa, we performed a flowback experiment by injecting carrier fluid at flow rates ranging from 100 to 300 ml/min.

2.3. Image Analysis

Light transmission techniques allowed us to accurately measure the fracture aperture field, b_{ij}. We acquired two reference images, one with the fracture filled with deionized water and one with the fracture filled with dyed water at a known concentration. The raw intensities were used to calculate the absorbance field using the Beer-Lambert law, $A_{dye} = \ln(\frac{I_c}{I_d})$, where I is the light intensity and subscripts c and d denote the clear and dyed solution, respectively. Using the Beer-Lambert law, absorbance was related to the aperture field by using an independently measured mean aperture; for more details see Detwiler et al. (1999)

$$b_{ij} = \frac{A_{dye_{ij}}}{\langle A_{dye} \rangle} \langle b \rangle \tag{2}$$

where b_{ij} is the aperture at fracture location (i,j), A is the absorbance and $\langle \cdot \rangle$ is a spatial average. The mean and standard deviation (in parenthesis) of the initial aperture was 3.114 mm (0.116), 2.865 mm (0.174), and 2.692 mm (0.110) in Tests A, B, and C, respectively. Note that the standard deviation reflects small long wavelength variations in the initial fracture aperture.

2.4. Solid Volume Fraction Measurement

Using light absorbance and scattering theory for a *slab* of particles (Bohren & Huffman, 2008), we derived a relationship for light absorbance as a function of ϕ_s within the fracture as

$$A = \phi_s \alpha_s b \tag{3}$$

where b is the fracture aperture, $A = \ln(\frac{I_{cf}}{I_s})$ is the absorbance, I_{cf} is the light intensity transmitted through the carrier fluid, I_s is the light intensity transmitted through the sand/carrier fluid mixture, and $\alpha_s = C_{ext\,s}/V_s$ is the light absorbance coefficient, for example, absorbance per unit length. The absorbance coefficient is the ratio of the extinction cross-section $C_{ext\,s}$ (a measure of total light attenuated) to the actual volume of the sand particles, V_s; thus, α has units of $length^{-1}$.

Using equation (3), we measured the absorbance coefficient of sand by carrying out a settling experiment. We prepared a concentrated ($\phi_s = 0.5$) suspension of silica sand (40/70 mesh) using a procedure similar to that described in section 2.2. The suspension was injected into a uniform aperture fracture and allowed to settle undisturbed for 6 days, which ensured settling reached steady state. Because the sand particles settled undisturbed (without shaking or vibration), we assumed that the settled solid concentration inside the fracture reached a value close to the random loose packing limit, $\phi_s \rightarrow \phi_{rlp} \approx 0.55$ (Shapiro & Probstein, 1992) and $\alpha_s \approx A_{ij}/(\phi_{rlp} b_{ij})$. The mean absorbance coefficient of 40/70 mesh silica sand was $\langle \alpha_s \rangle = 1.3$ mm^{-1} with a standard deviation of $\sigma_{\alpha_s} = 6.9 \times 10^{-2}$.

Light absorption scales linearly with all components attenuating light (Bohren & Huffman, 2008); therefore, light absorbance through the sand and fiber suspension scales as
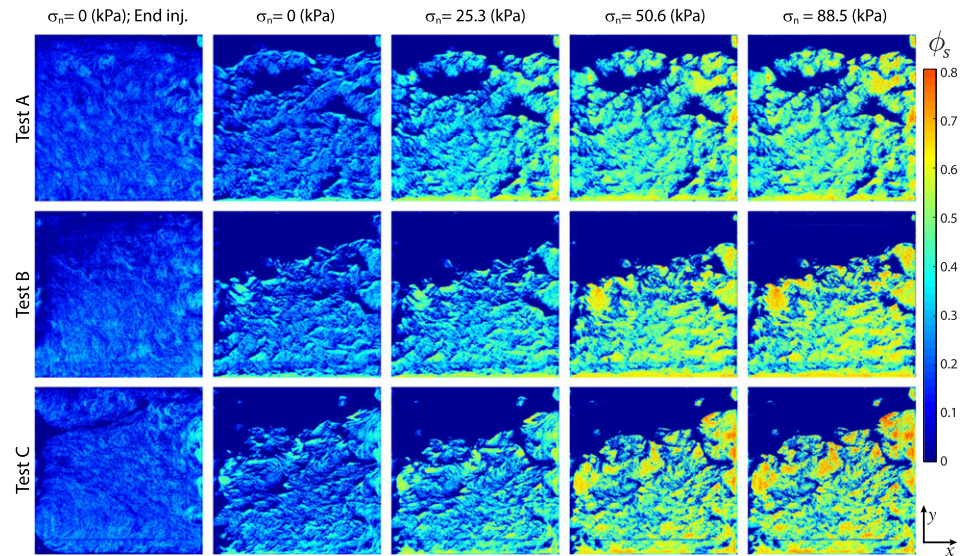
$$A = \phi_s \alpha_s b + \phi_f \alpha_f b \tag{4}$$

Figure 3. Solid volume fraction (ϕ_s) distribution for Tests A–C. As the applied stress increased, the solids are compacted and the stress is transferred from the boundaries to the solids. The compacted solids at the higher σ_n act as pillars, which prevent full fracture closure. The suspension was injected in the positive x direction, and gravity acted in the negative y direction.

where the subscripts s and f denote the sand and fiber, respectively, and the absorbance coefficient of fibers was defined as $\alpha_f = C_{\mathrm{ext}\,f}/V_f$, where $C_{\mathrm{ext}\,f}$ is the extinction cross section of fibers and V_f is the volume of a fiber particle. Both sand and fiber particles are much larger than the wavelength of the light source; therefore, we can use scaling arguments from Mie scattering theory to assume that $C_{\mathrm{ext}\,s}/a_{\mathrm{proj}\,s} \approx C_{\mathrm{ext}\,f}/a_{\mathrm{proj}\,f}$, where a_{proj} is the projected area of the particle, normal to the incident light. We assumed the projected area of fiber and sand particles to be that of a rectangle ($a_{\mathrm{proj}\,f} = l_f d_f$) and circle ($a_{\mathrm{proj}\,s} = \pi r^2$), respectively. The light absorbance of fibers can, therefore, be estimated using the independently measured α_s as

$$\alpha_f = \langle \alpha_s \rangle \frac{a_{\mathrm{proj}\,f}}{a_{\mathrm{proj}\,s}} \frac{V_s}{V_f} = \langle \alpha_s \rangle \frac{16r}{3\pi d_f} \tag{5}$$

where sand particles are approximated as spheres and fiber particles as cylinders. Due to the heterogeneity of fiber suspensions (e.g., flocculation), it was difficult to estimate the local fiber concentration using our experimental system. We used a first-order approximation of the local fiber concentration by calculating the total area covered by solids and assumed that fibers were uniformly distributed in these regions and absent from solids-free regions: in solids-free regions $\phi_f^* = 0$ and in regions where solids were found, we set $\phi_f^* = \phi_f/a_{\mathrm{solids}}$; here a_{solids} is defined as the fraction of the total area identified as having solids. Using the above analysis and assumptions yields

$$\phi_s = \frac{A - \alpha_f \phi_f^* b}{\alpha_s b} \tag{6}$$

where α_s was measured in the constant aperture experiment, α_f was estimated using equation (5), A was measured using light transmission techniques, and b was calculated by adjusting the aperture field based on recorded displacements by the LVDTs. A, b, ϕ_s, and ϕ_f^* in equation (6) vary within the fracture, while α_s and α_f are constants. This analysis yields a robust quantitative measure of the volume fraction of sand (ϕ_s) and gives a measure of the evolution of ϕ_s throughout the duration of the experiment. Figure 3 shows a snapshot (subset) of these ϕ_s fields at different times throughout the experiments.

3. Results

In this section, we present the experimental results of the initial suspension injection and settling, fracture displacement, and solid volume fraction changes due to the applied normal stress. We then present the experimental results of fluid flowback. We used the resulting solid distribution from the experiments to model fluid flowback using the numerical formulation presented in the supporting information.
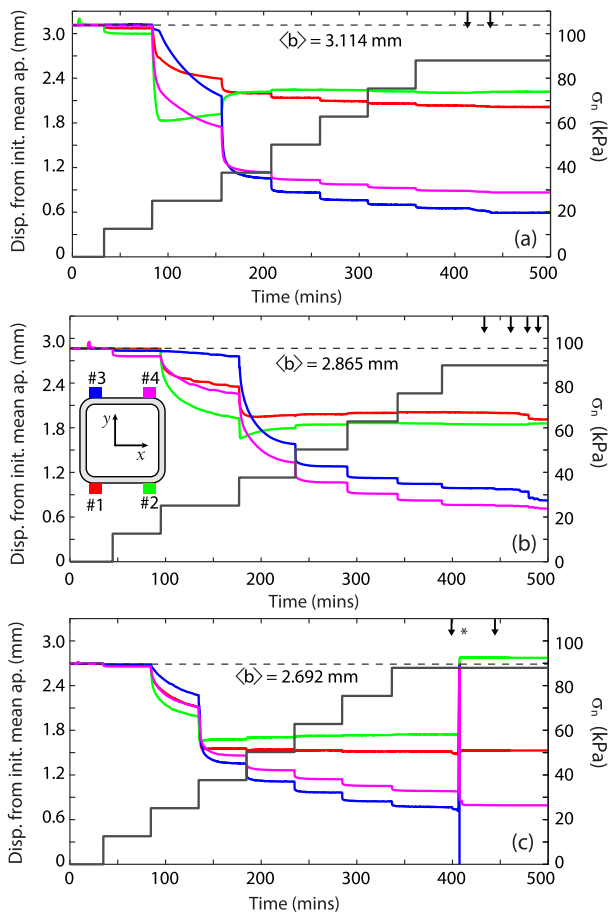
Figure 4. Fracture aperture reduction as σ_n increased. Panels (a)–(c) show displacement data for Tests A–C, respectively. The black line shows the applied normal stress, and the colored lines correspond to the linear variable displacement transducer locations as indicated in Figure 2 and shown in the inset in panel (b).

3.1. Initial Flow and Settling

The sand-fiber suspension was injected into the fracture at a flow rate of approximately 400 ml/min for about 5 min. Following the initial injection, flow stopped, and the solids settled uninterrupted (without an applied stress) for ~25 min. The ϕ_s fields in all experiments showed a similar solid distribution immediately after the suspension was injected into the fracture (first column in Figure 3). These ϕ_s fields show that the suspension was dispersed throughout the entire fracture, and the solids were heterogeneously distributed. This heterogeneity was due to the formation of sand-fiber clumps or aggregates resulting from the relatively high ϕ_s (compared to ϕ_f), which reduced the space between fiber particles and increased the probability of contact between fibers. The ϕ_s fields show that these clumps had a higher solid concentration ($\phi_s \approx 0.25$) than the initial solid concentration ($\phi_{total} \approx 0.18$).

The uninterrupted settling period led to significant differences in ϕ_s distribution compared to the initial distribution (second column in Figure 3). The ϕ_s fields suggest that there was differential settling between sand-fiber clumps and sand particles not interlocked in the clumps. That is, the sand-fiber clumps were immobilized; for example, they were trapped or jammed between the fracture walls. Because the fracture walls were smooth, immobilization suggests that these clumps were supported solely by shear stresses between the solids and the fracture walls. Sand particles not interlocked inside sand-fiber clumps settled at a significantly faster rate; however, some particles settled on top of the immobilized sand-fiber clumps. This settling process resulted in a heterogeneous ϕ_s field with the sand-fiber clump regions having significantly higher solid content and some solids-free regions randomly scattered around the sand-fiber clumps. During this uninterrupted settling phase, most solids from the top region of the fracture settled toward lower regions, which led to the formation of a large gap or channel near the top of the fracture. At the end of the initial settling phase, the clumps reached a sand concentration of $\phi_s \sim 0.25$ to 0.35; there were also visible solids-free pockets ($\phi_s = 0$) surrounding these clumps.

3.2. Solid Volume Fraction and Fracture Closure Due to Applied Stress

After the uninterrupted settling phase, we investigated the response of the sand-fiber proppant to an applied stress, simulating the shut-in phase of hydraulic fracturing. The normal stress was increased by 12.6 kPa every ~50 min up to a maximum of $\sigma_n = 88.5$ kPa with the fluid pressure maintained at ~4.5 kPa. The LVDTs securely mounted on the top aluminum frame measured the displacement of the top fracture surface. Figure 4 shows the LVDT displacements relative to the initial mean fracture aperture, $\langle b \rangle$. During the initial injection of the suspension, the mean fracture aperture increased by ~0.05–0.10 mm in all three experiments. After suspension injection stopped, the fracture aperture returned to its initial position (± 0.003 mm); the uninterrupted settling phase had no effect on the fracture aperture.

LVDT displacements show that applying a normal stress to the fracture reduced the fracture aperture. Figure 4 shows that the fracture aperture decreased $\lesssim 0.10$ mm after the normal stress was increased to $\sigma_n = 12.6$ kPa. Increasing σ_n from 25.3 to 37.9 kPa caused the fracture aperture in all three experiments to decrease significantly (~ 1.5 mm). The fracture aperture decreased by ~ 0.10 mm, after every σ_n step increase higher than 37.9 kPa. Furthermore, as σ_n increased, the aperture decreased nonuniformly, that is, the aperture on the upper region of the fracture (LVDTs 3 and 4) decreased more than the aperture near the bottom of the fracture (LVDTs 1 and 2). This nonuniform aperture reduction was likely due to the relatively low solid content in the upper regions of the fracture and resulted in an aperture decrease of ~85% in the upper region and ~40% in the lower region of the fracture. Figure 5a shows that as σ_n increased the mean aperture decreased significantly, reaching a 55% reduction at the highest applied normal stress. Though the aperture decreased
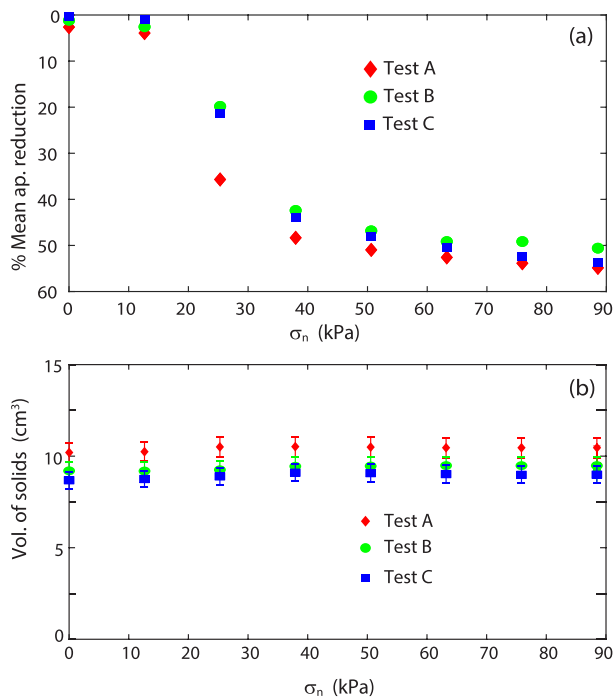
Figure 5. (a) Percent mean aperture reduction, relative to the initial mean aperture. As σ_n increased, the mean aperture decreased significantly. At the highest applied normal stress, the mean aperture decreased up to 55% in all three experiments. (b) Average volume of solids at the end of each applied normal stress step. Conservation of volume suggests that our analysis for the approximation of ϕ_s was valid.
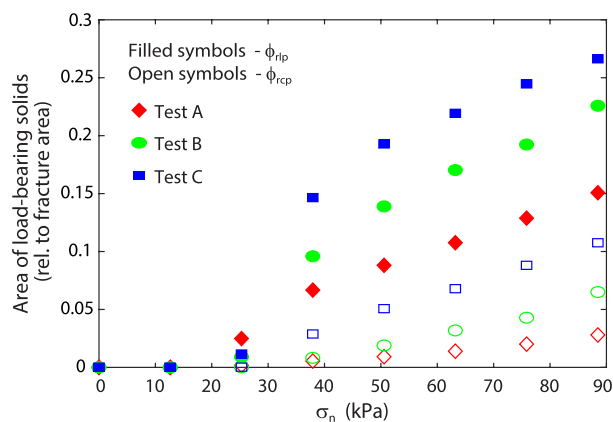

Figure 6. Area of load-bearing regions (relative to the fracture area). As the applied normal stress increased, the area of load-bearing regions increased which was due to compaction and spreading. Filled symbols: load-bearing ϕ_s set equal to $\phi_{rlp} = 0.55$. Open symbols: load-bearing ϕ_s set equal to $\phi_{rcp} = 0.64$. At the end of the experiments, the area covered by all solids was 174 (Experiment A), 144 (Experiment B), and 151 cm^2 (Experiment C). The fracture area was 232 cm^2.

significantly due to the applied stress, the fracture remained open, which suggests that some (if not all) solids were supporting the applied stress.

The results show that as σ_n increased, the fracture aperture decreased, which caused a significant increase in ϕ_s. The procedure to estimate ϕ_s using optical measurements was based on the assumption that total absorbance is linearly proportional to the absorbance of all components, for example, sand, fibers, and fluid (section 2.3). Furthermore, based on scaling arguments, we assumed that the unknown optical properties of fibers (α_f) could be derived from the measured optical properties of sand (α_s). Though both of these assumptions were reasonable (Bohren & Huffman, 2008), it was important to quantify the relative error associated with our ϕ_s estimates. Performing an uncertainty analysis, we found the relative error of our ϕ estimates to be 6% (see supporting information for more details). Furthermore, we verified that the procedure was accurate by performing a mass balance of the solids inside the fracture. Using the ϕ_s fields and known aperture fields, we estimated the volume of solids inside the fracture as σ_n increased. Figure 5b shows that the total volume of sand was conserved in all experiments. These results show that although the ϕ_s fields exhibited large changes in response to the aperture decrease induced by the increased σ_n, the volume of solids inside the fracture remained constant. The low relative uncertainty and the constant volume of solids inside the fracture suggest the assumptions made when deriving the ϕ_s estimates were adequate for this analysis.

At the end of the experiments, ϕ_s fields showed a highly heterogeneous solid distribution throughout the fracture (last column in Figure 3). In addition to the heterogeneous solids placement within the fracture, there was heterogeneity in solid concentration, for example, not all solids had the same ϕ. This ϕ_s heterogeneity resulted from the aperture decrease, which caused rearrangement of sand particles, and a corresponding decrease in void space between the solids or local increase in ϕ_s. Figure 3 shows that most solids had a concentration higher than the initial solid content of the suspension. As σ_n increased, some clumps reached $\phi_s \sim 0.6$ to 0.65, whereas some sand-fiber clumps in the top regions of the fracture had slightly higher solid concentration, $\phi_s \sim 0.75$ which was a result of the nonuniform displacement of the top fracture surface. The high ϕ_s values confirm that the fiber clumps were interlocked with sand particles, which compacted as the aperture decreased.

The solid volume fraction can be used as an indicator of the solids' ability to support an externally applied load. As ϕ_s increases, the probability of a particle being in contact with more than one particle increases. As the void space between particles decreases, the solids may reach a stable configuration capable of supporting an externally applied load. The concentration at which this stable configuration occurs is the jamming transition or the point at which the behavior of suspended solids transitions from fluid like to solid like. This transition occurs at a concentration between the random loose packing limit (ϕ_{rlp}) and the random close packing limit (ϕ_{rcp}; Santiso & Müller, 2002; Shapiro & Probstein, 1992). For uniform-sized spheres $\phi_{rlp} \approx 0.55$ and $\phi_{rcp} \approx 0.65$, while for nonspherical polydisperse particles $\phi_{max} \approx 0.84$ (Onoda & Liniger, 1990; Santiso & Müller, 2002). The ϕ_s fields suggests that some solids reached a solid concentration and thus a stable configuration, allowing these solids to support the applied normal stress and prevent the full closure of the fracture aperture.

We calculated the area of solids supporting the applied normal stress, that is, *load-bearing* solids, by applying a threshold to the ϕ_s fields: all locations with ϕ_s greater than some critical solid content, ϕ_c, were considered load bearing. Figure 6 shows the area of load-bearing solids relative to the
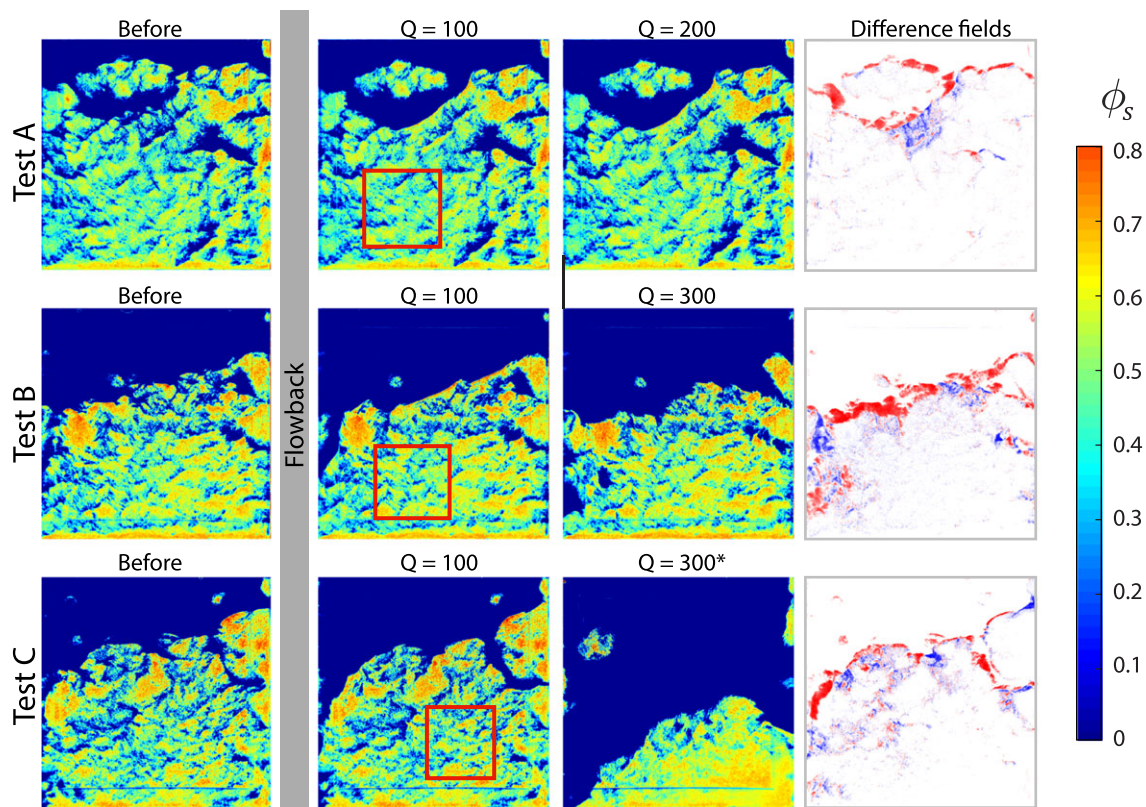
Figure 7. The ϕ_s distribution for Tests A–C, before and after flowback. In all cases $\sigma_n = 88.5$ kPa. Most fluid flowed through the large open channel near the top of the fracture. Flowback caused some solids to be mobilized and created wider channels. The difference fields show that solids were mostly mobilized from the edges surrounding the large channel near the top of the fracture. In Test C a large change in pore pressure caused solids to rearrange; see text for details. The red boxes identify regions used for the subregion simulations discussed in section 4; the simulations discussed in section 3.3.1 use the entire domain shown here.

fracture area (232 cm^2) for two values of ϕ_c, for example, $\phi_c = \phi_{rlp}$ (filled symbols) and $\phi_c = \phi_{rcp}$ (open symbols). Initially, there were no load-bearing solids, only after σ_n was increased to 25.3 kPa did a small fractions of solids become load bearing (Figure 6); note that this was also the stress at which the large decrease in aperture was recorded (see Figure 4). As σ_n increased, the area of load-bearing solids increased linearly (Figure 6). At the end of the experiment, load-bearing solids covered 3% to 15% (Test A), 7% to 23 % (Test B), and 11% to 27% (Test C) of the fracture. Note that these ranges are for ϕ_{rcp} and ϕ_{rlp}. The observed increase in area covered by load-bearing regions suggests that the sand-fiber pillars may be undergoing particle rearrangement, compaction, and spreading as the normal stress was increased.

3.3. Experimental Flowback
After solids had settled at the maximum stress ($\sigma_n = 88.5$ kPa), we conducted a flowback experiment by injecting solids-free carrier fluid at flow rates ranging from 100 to 300 ml/min. Fracture displacements recorded by the transducers show that the fluid injection had little effect on the fracture aperture in all experiments. In Test A, we performed two separate injections at a flow rate of 100 and 200 ml/min; in Test B four injections at a flow rate of 100, 100, 200, 300 ml/min; and in Test C two injections at a flow rate of 100 and 300 ml/min. Note that the black arrows on the top of each panel in Figures 4a–4c indicate the injection of carrier fluid during flowback. In all three experiments, the LVDTs displaced approximately 0.010 to 0.020 mm after each flowback injection. After 5 min of injection in Test C, the outlet tube was inadvertently blocked, which led to a temporary increase in pore pressure resulting in a significant increase in aperture (large vertical displacements observed in Figure 4c). This change in pore pressure and aperture caused significant changes in ϕ_s distribution with a significant amount of solids flushed out of the fracture (bottom right panel in Figure 7). Subsequent fluid injection at $Q = 300$ ml/min had no effect on the rearranged solid distribution.

In addition to the relatively small changes in aperture, flowback through the heterogeneous solid distribution caused some solids to be mobilized and flushed out of the fracture. Solid mobilization was mostly observed in the area near the top of the fracture, in regions adjacent to the large solids-free region of the fracture. Images
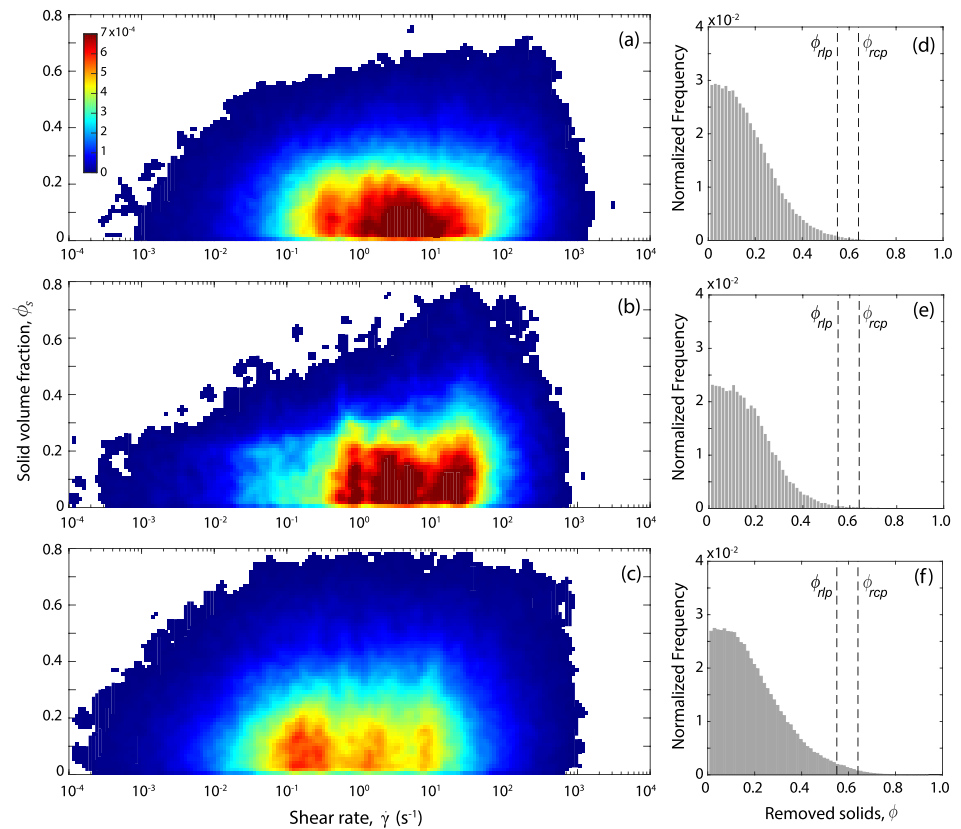
Figure 8. Joint probability distribution of $\dot{\gamma}$ and ϕ_s of solids mobilized during flowback in Tests A–C, shown in panels (a)–(c), respectively. The shear rate, $\dot{\gamma}$, at each location within the fracture was determined through full-field flow simulations through the measured ϕ_s fields (see Figure 7 for representative examples). The color scale is the normalized frequency of mobilized solids locations. There appears to be a strong correlation between the mobilized solids' concentration and the shear rates generated by fluid flowback. Most solids were mobilized by the larger shear rates, whereas the lower shear rates only tend to mobilize the low-ϕ_s solids. Panels (d)–(f) show normalized histograms of the concentration (ϕ_s) of mobilized solids in Tests A–C, respectively.

recorded during the flowback suggest that mobilization was mainly caused by the gradual erosion from the edges of pillars. In addition to the erosion, a few small isolated pillars ($\sim$5 mm $\times$ 5 mm) were also mobilized during flowback.

Figure 7 shows the ϕ_s distribution before and after flowback for all experiments. Solid mobilization caused the widening of the large open channels; this widening can be seen in more detail by looking at the difference in solid content before and after flowback. The last column in Figure 7 shows the difference field before and after the last flowback flow rate, for example, at the end of $Q = 200$, $Q = 300$, and $Q = 100$ ml/min for Tests A, B, and C, respectively. Red represents locations where solids were eroded, and blue shows locations where solids were deposited. Approximately 0.4 (A), 0.9 (B), and 2.9 cm^3 (C) were flushed out of the fracture during flowback in Tests A, B, and C, respectively. Additionally, the area of load-bearing solids relative to the area occupied by all solids increased after flowback in all experiments, which suggests that most mobilized solids were not load bearing. In Test C, one third of the total solids were flushed out of the fracture; the remaining solids were rearranged into a compact sand pack at the bottom of the fracture (third panel in Figure 7).

The results from flowback experiments suggest that the wide channels near the top acted as high-permeability conduits, which caused flow to be focused through these channels with relatively little flow passing through the sand pack. This apparent flow focusing led to the mobilization of solids in the regions adjacent to the channel creating wider channels. There were no significant changes in solid distribution, and minimal solid mobilization was observed in the bottom half of the fracture (within the sand pack). We hypothesized that there were two competing mechanisms controlling solid mobilization: the shear stress exerted by the fluid on the side of the pillars causing solid erosion and mobilization acting against
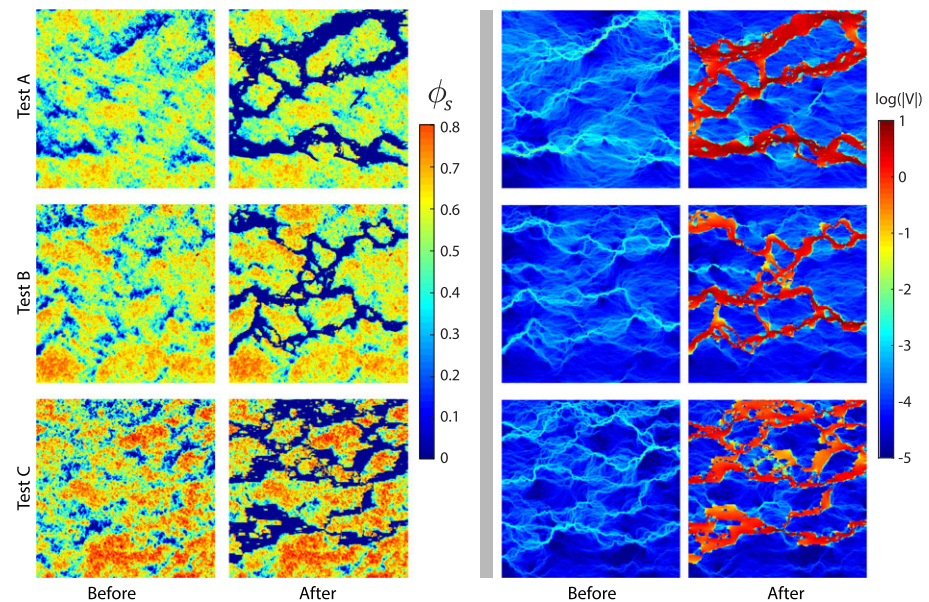
Figure 9. Simulation results showing the development of high-transmissivity channels due to solid mobilization. The first and second columns show the ϕ_s distribution before and after mobilization. The third and fourth columns show the velocity magnitude, $|V|$, before and after erosion. The sand pack region for these simulations is highlighted in Figure 7.

the applied normal stress (e.g., contact stress between particles) preventing solids mobilization. We cannot directly measure shear stresses within the fracture during experiments; however, we can use flow simulations through the measured flow geometry to estimate the magnitudes of local shear stresses.

3.3.1. Numerical Simulation of Flowback

We investigated solid mobilization due to flowback by simulating solids-free carrier fluid injection through the solid distribution at the end of the experiments. Here we provide a brief overview of the model (for a more detailed description and a link to the source code; see the supporting information), which represents flow of an Ellis fluid through a parallel-plate fracture with localized regions occupied by sand, where ϕ_s in the modeled sand-filled regions ranged between 0 and ϕ_{max}. The numerical model is similar to a parallel-plate fracture with localized contacts (e.g., Jasinski & Dabrowski, 2018), but here the contacts are permeable. Flow through the permeable sand pack was simulated as Darcy flow through a porous medium (de Castro & Radilla, 2017; Tosco et al., 2013). Due to the low Reynolds numbers ($Re \ll 1$), inertial forces and other nonlinear flow effects were ignored. The permeability at each cell was calculated as the geometric average of permeability of a porous matrix and parallel fracture. The resulting nonlinear flow equation was solved using Picard iteration. We simulated flow through the heterogeneous ϕ_s distribution in our experiments by applying a constant pressure at the inlet (left) and outlet (right) and no-flux boundary on the top and bottom of the fracture and solving for the velocity field. The simulations for Tests A–C all show that the top of the fracture had the highest velocity, which confirmed that flow was focused through the large open channel as discussed. The sand pack in the bottom regions of the fracture experienced significantly lower flow; velocity in the sand pack was several orders of magnitude smaller than velocity in the channel. Additionally, the simulations revealed that fluid moves significantly faster, by 2 orders of magnitude, through the solids-free regions than fluid through the sand-fiber pillar regions.

We tested the hypothesis that solid mobilization was induced by shear stresses exerted by the fluid and inhibited by contact stresses between particles by constructing a time history of the velocity field within the entire flow field during flowback. This time history was constructed by solving the steady state velocity field for each experimentally measured ϕ_s field during flowback. These velocity fields provided estimates of shear rate, $\dot{\gamma} = \left((\frac{du}{dy})^2 + (\frac{dv}{dx})^2 \right)^{1/2}$, throughout the fracture. For each time step, we identified the locations from which sand was mobilized and recorded ϕ_s and $\dot{\gamma}$ at each of these locations. Figure 8 shows the joint probability distribution of ϕ_s and $\dot{\gamma}$ of mobilized regions constructed over the duration of the flowback process. Figure 8 suggests a strong correlation between $\dot{\gamma}$ generated by fluid flowback and solid mobilization: most solids were mobilized by $\dot{\gamma}$ between 0.1 and 100 s^{-1}. Furthermore, it appears that there is a critical $\dot{\gamma}_{mob}$ required to mobilize solids. Histograms of ϕ_s for mobilized solids show that a large fraction of mobilized solids had a low
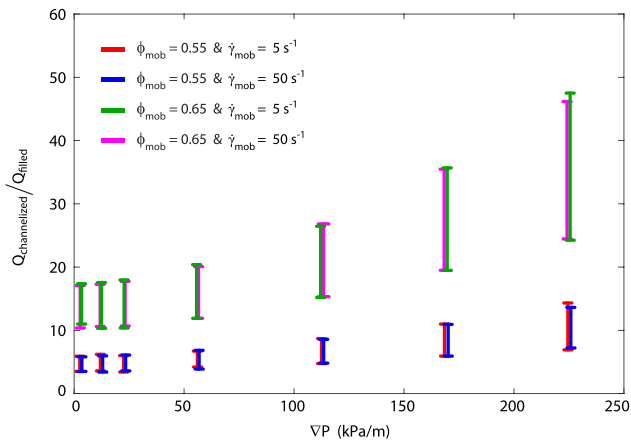
Figure 10. Flow rate through channelized solid distribution, normalized by the flow rate through the same fracture filled with a uniform solid content. The bars show the variability between results for the different ϕ_s distributions (e.g., Tests A–C).

concentration (Figures 8d–8f). These results suggest that indeed, the two mechanisms controlling solid mobilization are the shear rates generated by the fluid and the normal forces between load-bearing solids. Figure 8 suggests that the main mechanism of mobilization was erosion caused by the high $\dot{\gamma}$ at the fluid-solid boundary of the sand-fiber pillars. Erosion was observed in the acquired images and is supported by the high amount of mobilized solids with low ϕ_s values. Furthermore, the normalized histograms suggest that solid mobilization is unlikely to occur when solids reach a concentration above some ϕ_{mob}; this concentration seems to be between ϕ_{rlp} and ϕ_{rcp} (Figures 8d–8f).

4. Discussion

The experimental procedure and relatively small scale of the fracture led to the formation of a large channel near the top of the fracture. During flowback, flow was focused through this channel with relatively little flow through the sand pack in the bottom approximately two thirds of the fracture. In field-scale applications, proppant is typically injected radially from a wellbore into a vertical fracture propagating from the wellbore. Thus, it is likely that large-scale channels such as those observed in our experiments will form far from the well bore and may have a negligible impact on fluid flow to the well. To investigate the potential impact of solid mobilization in the absence of such large-scale preferential channels, we simulated flow through a small (5.2 cm^2) region inside the sand pack (red box in Figure 7). Though the ϕ_s distribution is heterogeneous, the initial ϕ_s distribution lacks a single dominant preferential flow path. The simulations were carried out by applying constant pressure on the left and right sides of the field and no-flux boundaries on the top and bottom of the field.

The flow simulations provided local measurements of $\dot{\gamma}$ throughout the flow field. We then identified locations meeting the mobilization condition, $\phi_s < \phi_{mob}$ and $\dot{\gamma} > \dot{\gamma}_{mob}$, and artificially mobilized the solids at those locations by setting $\phi_s = 0$. The velocity field was solved again using the new ϕ_s field, repeating the process until the flow and ϕ_s fields reached a steady state. Note that we only simulated mobilization and did not consider the possibility of particle deposition. Figure 9 shows the steady state ϕ_s fields and velocity fields before and after artificial solid mobilization for $\phi_{mob} = 0.55$, $\dot{\gamma}_{mob} = 0.5$ s^{-1}, and $\nabla P = 224$ kPa/m. The simulation results show that artificial mobilization led to the formation of high-transmissivity channels that grew from the high-$\dot{\gamma}$ regions in the thin preferential flow paths within the sand pack. As solids were mobilized channels developed and widened until the shear rate at the edge of the channel was lower than $\dot{\gamma}_{mob}$ or until the edge of the channel edge reached a region with $\phi_s \geq \phi_{mob}$. These simulations show that solid erosion and mobilization may lead to the formation of channels within the heterogeneous sand pack which may significantly increase fracture transmissivity.

We explored the effect of varying the mobilization threshold on the artificial mobilization. We simulated artificial mobilization for a range of mobilization thresholds: $\dot{\gamma}_{mob} = 5.0$ to 50.0 s^{-1} with $\phi_{mob} = \phi_{rlp} = 0.55$ or $\phi_{mob} = \phi_{rcp} = 0.65$, over a wide range of pressure gradients, $\nabla P = 22.4 - 224$ kPa/m. We calculated the flow rate through the channelized or artificially eroded fracture ($Q_{channelized}$) and normalized by the flow rate of a fracture filled with a uniform $\phi_s = \phi_{mob}$ sand pack (Q_{filled}). Note that even before solid mobilization, flow through a heterogeneous ϕ_s distribution was higher than flow through uniform ϕ_s sand pack. Figure 10 shows the normalized flow rates for different mobilization thresholds; the bar shows the variability between experiments. The results suggest that solid mobilization was more sensitive to ϕ_{mob}. For the conditions tested here, flow through the heterogeneous and eroded ϕ_s distribution was 5 to 48 times higher than the flow through a fracture filled with uniformly distributed solids. Solid mobilization in these simulations resulted in the formation of channels ranging from 0.2 to 3.2 mm wide. These simulations suggest that solid mobilization may lead to a significant increase fracture transmissivity.

5. Conclusions

We presented experiments in which sand-fiber proppant mixtures were injected into a vertical, deformable, and transparent analog fracture. We extended transmitted light techniques to measure the volumetric

ratio, ϕ_s, of solids throughout the fracture. The resulting complex settling behavior led to the formation of sand-laden fiber agglomerates (e.g., sand-fiber clumps). Increasing the applied normal stress on the fracture surfaces caused fracture closure until some of the sand-fiber clumps reached a critical solid content, ϕ_c, and supported the applied stress. Despite reductions of up to 55% from the initial mean aperture, at the highest applied stress, the load-bearing solids covered only 15% to 25% of the total fracture area. Subsequent flow-back of solids-free carrier fluid mobilized solids from low-ϕ_s regions and widened solids-free channels through the fracture. Comparisons of simulations of flow through a completely sand-filled fracture to simulations in the fiber-induced heterogeneous solid distributions observed in the experiments suggest order-of-magnitude improvements in resulting fracture transmissivity.

Creating and maintaining transmissivity through injection of proppants into induced fractures is a resource-intensive process requiring large quantities of sand and water (e.g., Edwards & Celia, 2018). The experimental results presented here suggest that the addition of small amounts of polymeric fibers to suspended proppants can reduce the amount of sand required while significantly increasing the resulting fracture transmissivity. For example, to prop a fracture with a mean aperture of 1.5 mm using a uniform proppant distribution (i.e., conventional approach using only sand as the proppant) would require ~65% more sand than was required during our experiments with fibers added to the proppant suspension, and the fracture propped by heterogeneous sand-fiber clumps will have significantly higher transmissivity than the sand-filled fracture. Furthermore, because the effective viscosity of the suspension is strongly dependent on the volume ratio of sand in the suspension and the relative ratio of fibers to sand, introducing a small fraction of fibers and reducing the sand content to one third of a high-solids content sand-only suspension leads to a significant reduction in effective viscosity; this has the additional advantage of reducing energy requirements for pumping the lower-solids content suspension.

Our experimental results demonstrate potentially significant advantages to incorporating fibers into proppant suspensions, but several outstanding challenges must be addressed to more accurately quantify these benefits. We applied a simplified model that used the observed correlations between shear stress and solid volume fraction to trigger solid mobilization. We assumed that mobilized solids flowed freely from the fracture, which was consistent with our experimental observations. However, it is possible that there will be a scale dependence of the final distribution of sand-fiber clumps, which may influence both the mobilization of solids and the resulting preferential flow paths. In addition, in larger fractures, it is likely that an increasing fraction of mobilized solids may become immobilized elsewhere in the fracture. Development of mechanistic models of the solid settling and mobilization/immobilization processes could provide a means for exploring these questions related to the scalability of the benefits of including fibers in proppant suspensions.

References

Amundarain, J., Castro, L., Rojas, M., Siquier, S., Ramírez, N., Müller, A., & Sáez, A. (2009). Solutions of xanthan gum/guar gum mixtures: Shear rheology, porous media flow, and solids transport in annular flow. *Rheologica Acta*, *48*(5), 491–498. https://doi.org/10.1007/s00397-008-0337-5

Barbati, A. C., Desroches, J., Robisson, A., & McKinley, G. H. (2016). Complex fluids and hydraulic fracturing. *Annual Review of Chemical and Biomolecular Engineering*, *7*(1), 415–453. https://doi.org/10.1146/annurev-chembioeng-080615-033630

Bohren, C. F., & Huffman, D. R. (2008). *Absorption and Scattering of Light by Small Particles*. New York: John Wiley & Sons.

Bulova, M. N., Nosova, K. E., Willberg, D. M., & Lassek, J. T. (2006). In *SPE Annual Technical Conference and Exhibition, Society of Petroleum Engineers, San Antonio, Texas, USA*, Benefits of the novel fiber-laden low-viscosity fluid system in fracturing low-permeability tight gas formations. https://doi.org/10.2118/102956-MS

Chudzikowski, R. J. (1971). Guar gum and its applications. *Journal of the Society of Cosmetic Chemists*, *22*(1), 43–60.

de Castro, A. R., & Radilla, G. (2017). Non-Darcian flow of shear-thinning fluids through packed beads: Experiments and predictions using Forchheimer's law and Ergun's equation. *Advance Water Resources*, *100*, 35–47. https://doi.org/10.1016/j.advwatres.2016.12.009

Detwiler, R. L., Pringle, S. E., & Glass, R. J. (1999). Measurement of fracture aperture fields using transmitted light: An evaluation of measurement errors and their influence on simulations of flow and transport through a single fracture. *Water Resources Research*, *35*(9), 2605–2617. https://doi.org/10.1029/1999WR900164

Economides, M., & Nolte, K. (2000). *Reservoir Stimulation* (2nd ed.). New Jersey: Prentice Hall Englewood Cliffs.

Edwards, R. W. J., & Celia, M. A. (2018). Shale gas well, hydraulic fracturing, and formation data to support modeling of gas and water flow in shale formations. *Water Resources Research*, *54*, 3196–3206. https://doi.org/10.1002/2017wr022130

Elgaddafi, R., Ahmed, R., George, M., & Growcock, F. (2012). Settling behavior of spherical particles in fiber-containing drilling fluids. *Journal of Petroleum Science and Engineering*, *84-85*, 20–28. https://doi.org/10.1016/j.petrol.2012.01.020

Férec, J., Heuzey, M., Ausias, G., & Carreau, P. (2008). Rheological behavior of fiber-filled polymers under large amplitude oscillatory shear flow 4th Annual European Rheology Conference. *Journal of Non-Newtonian Fluid Mechanics*, *151*(1–3), 89–100. https://doi.org/10.1016/j.jnnfm.2008.01.002

George, M., Ahmed, R., & Growcock, F. (2011). Rheological properties of fiber-containing drilling sweeps at ambient and elevated temperatures. In *2011 AADE National Technical Conference and Exhibition American Association of Drilling Engineers*, Houston Texas.

George, M., Ahmed, R., & Growcock, F. (2012). Stability and flow behavior of fiber-containing drilling sweeps. In J. De Vicente (Ed.), *Rheology Chap 9*. Rijeka: InTech. https://doi.org/10.5772/35736. Retrieved from http://www.intechopen.com/books/rheology/stability-and-flow-behavior-of-fiber-containing-drilling-sweeps

Germanovich, L. N., & Murdoch, L. C. (2010). Injection of solids to lift coastal areas. *Proceedings of the Royal Society of London A*, *466*(2123), 3225–3252. https://doi.org/10.1098/rspa.2010.0033

Gillard, M. R., Medvedev, O. O., Hosein, P. R., Medvedev, A., Peñacorada, F., & d'Huteau, E. (2010). A new approach to generating fracture conductivity. In *SPE Annual Technical Conference and Exhibition Society of Petroleum Engineers*, pp. 19–22. https://doi.org/10.2118/135034-MS

Guo, R., Azaiez, J., & Bellehumeur, C. (2005). Rheology of fiber filled polymer melts: Role of fiber-fiber interactions and polymer-fiber coupling. *Polym Engineering and Science*, *45*(3), 385–399. https://doi.org/10.1002/pen.20285

Guo, J., Ma, J., Zhao, Z., & Gao, Y. (2015). Effect of fiber on the rheological property of fracturing fluid. *Journal of Natural Gas Science and Engineering*, *23*(0), 356–362. https://doi.org/10.1016/j.jngse.2015.02.017

Herzhaft, B., Guazzelli, E., Mackaplow, M. B., & Shaqfeh, E. S. G. (1996). Experimental investigation of the sedimentation of a dilute fiber suspension. *Physical Review Letters*, *77*, 290–293. https://doi.org/10.1103/PhysRevLett.77.290

Howard, P., James, S., & Milton-Tayler, D. (1999). High permeability channels in proppant packs containing random fibers. In *Society of Petroleum Engineers in SPE Formation Damage Control Conference*, pp. 3. https://doi.org/10.2118/57392-PA

Jasinski, L., & Dabrowski, M. (2018). The effective transmissivity of a plane-walled fracture with circular cylindrical obstacles. *Journal of Geophysical Research: Solid Earth*, *123*, 242–263. https://doi.org/10.1002/2017jb014509

Lei, C., & Clark, P. E. (2007). Crosslinking of guar and guar derivatives. *Society of Petroleum Engineers SPE Journal*, *12*(3), 316–321. https://doi.org/10.2118/90840-PA

Liu, Y., & Sharma, M. M. (2005). Effect of fracture width and fluid rheology on proppant settling and retardation: An experimental study. In *Society of Petroleum Engineers, SPE Annual Technical Conference and Exhibition Dallas*, Texas. https://doi.org/10.2118/96208-MS

Medina, R., Elkhoury, J. E., Morris, J. P., Prioul, R., Desroches, J., & Detwiler, R. L. (2015). Flow of concentrated suspensions through fractures: Small variations in solid concentration cause significant in-plane velocity variations. *Geofluids*, *15*(1-2), 24–36. https://doi.org/10.1111/gfl.12109

Medina, R., Elkhoury, J. E., Morris, J. P., Prioul, R., Desroches, J., & Detwiler, R. L. (2016). *Flow of Concentrated Suspensions Through Fractures: Small Variations in Solid Concentration Cause Significant In-plane Velocity Variations Chap. 5*. Chichester, UK: Wiley-Blackwell.

Medvedev, A. V., Kraemer, C. C., Pena, A. A., & Panga, M. K. R. (2013). *On the Mechanisms of Channel Fracturing*. The Woodlands, Texas, USA: Society of Petroleum Engineers in SPE Hydraulic Fracturing Technology Conference. https://doi.org/10.2118/163836-MS

Metzner, A. B. (1985). Rheology of suspensions in polymeric liquids. *Journal of Rheology*, *29*(6), 739–775. https://doi.org/10.1122/1.549808

Montgomery, C. (2013). Fracturing fluids. In A. P. Bunger, J. McLennan, & R. Jeffrey (Eds.), *Effective and Sustainable Hydraulic Fracturing*. Rijeka: InTech. https://doi.org/10.5772/56192. Retrieved from https://www.intechopen.com/books/effective-and-sustainable-hydraulic-fracturing/fracturing-fluids

Morris, J. P., Chugunov, N., & Meouchy, G. (2014). *Understanding Heterogeneously Propped Hydraulic Fractures Through Combined Fluid Mechanics, Geomechanics, and Statistical Analysis*. American Rock Mechanics Association.

Murdoch, L. C., Richardson, J. R., Tan, Q., Malin, S. C., & Fairbanks, C. (2006). Forms and sand transport in shallow hydraulic fractures in residual soil. *Canadian Geotechnical Journal*, *43*(10), 1061–1073. https://doi.org/10.1139/T06-063

Onoda, G. Y., & Liniger, E. G. (1990). Random loose packings of uniform spheres and the dilatancy onset. *Physical Review Letters*, *64*, 2727–2730. https://doi.org/10.1103/PhysRevLett.64.2727

Osiptsov, A. A. (2017). Fluid mechanics of hydraulic fracturing: A review. *Journal of Petroleum Science and Engineering*, *156*, 513–535. https://doi.org/10.1016/j.petrol.2017.05.019

Potapenko, D. I., Ramsey, L., Lesko, T. M., Willberg, D. M., Lafferty, T., & Still, J. W. (2014). Compositions and methods for increasing fracture conductivity.

Rajabian, M., Dubois, C., Grmela, M., & Carreau, P. (2008). Effects of polymer–fiber interactions on rheology and flow behavior of suspensions of semi-flexible fibers in polymeric liquids. *Rheologica Acta*, *47*(7), 701–717.

Santiso, E., & Müller, E. A. (2002). Dense packing of binary and polydisperse hard spheres. *Molecular Physics*, *100*(15), 2461–2469. https://doi.org/10.1080/00268970210125313

Schmid, C. F., Switzer, L. H., & Klingenberg, D. J. (2000). Simulations of fiber flocculation: Effects of fiber properties and interfiber friction. *Journal of Rheology*, *44*(4), 781–809. https://doi.org/10.1122/1.551116

Shapiro, A. P., & Probstein, R. F. (1992). Random packings of spheres and fluidity limits of monodisperse and bidisperse suspensions. *Physical Review Letters*, *68*, 1422–1425. https://doi.org/10.1103/PhysRevLett.68.1422

Shiozawa, S., & McClure, M. (2016). Simulation of proppant transport with gravitational settling and fracture closure in a three-dimensional hydraulic fracturing simulator. *Journal of Petroleum Science and Engineering*, *138*, 298–314. https://doi.org/10.1016/j.petrol.2016.01.002

Tosco, T., Marchisio, D. L., Lince, F., & Sethi, R. (2013). Extension of the Darcy-Forchheimer law for shear-thinning fluids and validation via pore-scale flow simulations. *Transport Porous Med.*, *96*(1), 1–20. https://doi.org/10.1007/s11242-012-0070-5

Vasudevan, S., Willberg, D. M., Wise, J. A., Gorham, T. L., Dacar, R. C., Sullivan, P. F., et al. (2001). Field test of a novel low viscosity fracturing fluid in the lost hills field, California, SPE Western Regional Meeting.

Willberg, D. M., Miller, M. J., Thiercelin, M. J., & Kosarev, I. V. (2011). Method for hydraulic fracturing of subterranean formation, US Patent 8061424, b2.